

Article

# CFD Simulation for Estimating Efficiency of PBCF Installed on a 176K Bulk Carrier under Both POW and Self-Propulsion Conditions

Dong-Hyun Kim <sup>1</sup>, Jong-Chun Park <sup>1,\*</sup>, Gyu-Mok Jeon <sup>1</sup> and Myung-Soo Shin <sup>2</sup>

<sup>1</sup> Department of Naval Architecture and Ocean Engineering, Pusan National University, Busan 46241, Korea; xdo2004@pnu.edu (D.-H.K.); comjys0675@pnu.edu (G.-M.J.)

<sup>2</sup> Korea Research Institute of Ships and Ocean Engineering, Daejeon 34103, Korea; msshin@kriso.re.kr

\* Correspondence: jcpark@pnu.edu

**Abstract:** In this paper, the efficiency of Propeller Boss Cap Fins (PBCF) installed at the bulk carrier was estimated under both Propeller Open Water (POW) and self-propulsion conditions. For this estimation, virtual model-basin tests (resistance, POW, and self-propulsion tests) were conducted through Computational Fluid Dynamics (CFDs) simulation. In the resistance test, the total resistance and the wake distribution according to ship speed were investigated. In the POW test, changes of thrust, torque coefficient, and open water efficiency on the propeller according to PBCF installation were investigated. Finally, the International Towing Tank Conference (ITTC) 1978 method was used to predict the effect of PBCF installation on self-propulsive coefficient and brake horsepower. For analyzing incompressible viscous flow field, the Reynolds-Averaged Navier–Stokes (RANS) equation with SST  $k-\omega$  turbulence model was calculated using Star-CCM+ 11.06.010-R8. All simulation results were validated by comparing the results of model tests conducted at the Korea Research Institute of Ships and Ocean Engineering (KRISO). Consequently, for the self-propulsion test with the PBCF, a 1.5% reduction of brake horsepower was estimated in the simulation and a 0.5% reduction of the brake horsepower was estimated in the experiment.

**Keywords:** Propeller Boss Cap Fins (PBCF); resistance test; Propeller Open Water (POW) test; self-propulsion test; Computational Fluid Dynamics (CFDs)



**Citation:** Kim, D.-H.; Park, J.-C.; Jeon, G.-M.; Shin, M.-S. CFD Simulation for Estimating Efficiency of PBCF Installed on a 176K Bulk Carrier under Both POW and Self-Propulsion Conditions. *Processes* **2021**, *9*, 1192. <https://doi.org/10.3390/pr9071192>

Academic Editor: Yonghwan Kim

Received: 14 June 2021

Accepted: 6 July 2021

Published: 9 July 2021

**Publisher's Note:** MDPI stays neutral with regard to jurisdictional claims in published maps and institutional affiliations.



**Copyright:** © 2021 by the authors. Licensee MDPI, Basel, Switzerland. This article is an open access article distributed under the terms and conditions of the Creative Commons Attribution (CC BY) license (<https://creativecommons.org/licenses/by/4.0/>).

## 1. Introduction

According to IMO (International Maritime Organization) and ICCT (The International Council on Clean Transportation), greenhouse gas emissions from ship operations account for about 3.1% of global emissions which amount to about 1 billion tons quantitatively [1,2]. In addition, Cames et al. [3] have predicted that 17% of global carbon dioxide emissions could be generated by ships by 2050 due to continuous increase in demand for ships as the current situation is maintained. IMO regulates the EEDI (Energy Efficiency Design Index), an index expressed by the calculation of carbon dioxide emissions at the ship design stage, to cope with environmental pollution problems of ships [4]. Since ships not satisfying EEDI standards cannot be built, many studies have recently been conducted to reduce EEDI.

There are three main ways to reduce EEDI: the use of eco-friendly fuels, the reduction of hull resistance, and the improvement of propulsion efficiency. PBCF (Propeller Boss Cap Fins) was developed in 1987 as one of the ESDs (Energy Saving Devices) in which the fuel consumption was reduced by improving the propeller propulsion efficiency. It has been installed on more than 2000 ships to date [5]. As shown in Figure 1, PBCF with the same number of small fins as the number of propeller blades on the divergence boss cap can reduce the energy loss of ship's propulsion system by disrupting the hub vortex which may be generated in the wake of the propeller by overlapping the accelerated flow

at the trailing edge of the propeller (Figure 2). As a result, the propeller thrust is increased whereas the torque is decreased so that the propeller efficiency is enhanced [6].



Figure 1. PBCF installed at propeller hub [6].

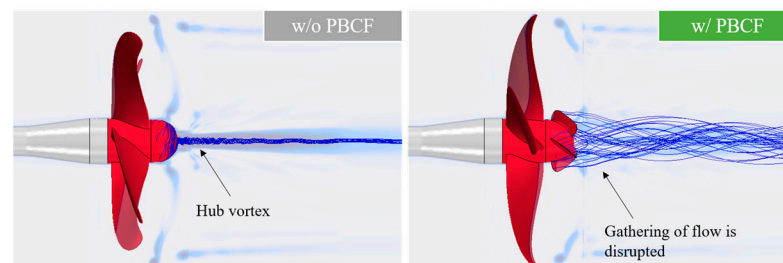


Figure 2. Hub vortex disappears by PBCF installation [7].

Ouchi et al. [8] have performed a POW (Propeller Open Water) test on the model-scale and reported that the increase of propeller open water efficiency due to PBCF is about 1–2%. Nojiri et al. [6] have performed shape optimization of PBCF, verified it from the model-scale POW test and CFD simulation, and finally obtained an efficiency of 1.5%. Kawamura et al. [5] have conducted simulation and model tests for PBCF under POW condition and obtained an efficiency of 1.5–2.5%. Ghassemi et al. [9] have performed BEM simulation under the same condition as Kawamura et al. [5] and confirmed the efficiency of PBCF as 1%. In addition, Druckenbrod et al. [10], Katayama et al. [11], Park et al. [12], and Mizzi et al. [13] have performed model-scale experiment and the CFD simulation for PBCF and reported that the efficiency of PBCF is in the range of 0.8–2%. However, all PBCF efficiencies estimated from these preceding studies were acquired under the POW condition at model-scale only.

However, the efficiency of PBCF estimated from POW test and CFD simulation at model-scale can show quite different trends from that of the full-scale measurement. Nojiri et al. [6] have announced that the delivered horsepower (DHP) is reduced by 2–10% due to PBCF according to analysis of full-scale measurement data and sea trial results of 16 ships equipped with various ESDs. Kawamura et al. [5] have reported that the PBCF, which provide about 2.5% efficiency in model tests under POW condition, produces more than 4% DHP reduction in the full-scale measurements. Ghassemi et al. [9] have also confirmed that the efficiency is increased only about 1% under the POW condition at the model-scale, which shows a 3.5–4% reduction in shaft DHP at sea trial. Katayama et al. [11] have announced that PBCF produces an average of 3% DHP reduction after analyzing data of the full-scale measurements over several months. Also, Kim et al. [14] have analyzed the performance of PBCF from the full-scale measurement and reported that PBCF could reduce the fuel consumption and the DHP by about 2.4% and 7.8%, respectively. From these preceding studies shown above, it is obvious that under full-scale and self-propulsion condition, PBCF has a distinct effect different from that of the model-scale and POW

condition. Therefore, in order to accurately estimate the effect of PBCF, it is necessary to consider the self-propulsion condition, the hull-rudder interaction, and the full-scale analysis. However, considering the full-scale effect by CFD simulation seems somewhat unreasonable at this moment in time.

Therefore, the purpose of this study was to perform a CFD simulation at the model-scale to estimate the efficiency of PBCF under both POW and self-propulsion conditions. At first, with the POW test, change rate of the thrust, the torque coefficient, and the propeller open water efficiency due to PBCF were estimated. The operation mechanism of PBCF was then analyzed. Secondly, resistance and self-propulsion tests were performed and the full-scale performance was estimated using the ITTC (International Towing Tank Conference) 1978 method. Finally, effects of PBCF on self-propulsion coefficient, brake horsepower (BHP) in self-propulsion condition were analyzed. All simulation results were validated by comparing results of a model test conducted in KRISO (Korea Research Institute of Ships and Ocean Engineering).

## 2. Test Methods

### 2.1. Resistance Test

Generally, the resistance test is performed to measure the resistance performance when a bare hull without a propeller goes forward at a constant speed. The resistance performance includes not only hull form resistance, but also the stern flow distribution for designing the propeller, which is called the nominal wake. The resistance test can be carried out with rudder and bilge keel if those are installed on the ship.

The resistance test is carried out by mounting the model ship on the carriage in the towing tank and moving the tank forward at a constant speed. The physical quantity that is directly measured includes the total resistance ( $R_T$ ) at a specific speed of the model ship and the nominal wake distribution that visualizes the flow distribution at the propeller generation line.

### 2.2. POW Test

The POW test is performed to measure the performance of the propeller alone under the condition in which the fluid flowing into the propeller is not disturbed by the hull. The POW test is mainly carried out by mounting a propeller on a carriage of the towing tank, rotating the propeller at a specific rps (revolution per second), and advancing the carriage by a target speed of the inflow.

Physical quantities that are directly measured in a POW test include the propeller's thrust ( $T$ ) and torque ( $Q$ ) according to the specific rps and the speed of inflow. The advance ratio ( $J$ ), the thrust coefficient ( $K_T$ ), the torque coefficient ( $K_Q$ ), and the open water propeller efficiency ( $\eta_O$ ) can be acquired from Equations (1)–(4), respectively. Ultimately, the POW curve representing the relationship of  $J$  with  $K_T$  and  $K_Q$  might be estimated.

$$J = \frac{V_A}{nD} \quad (1)$$

$$K_T = \frac{T}{\rho n^2 D^4} \quad (2)$$

$$K_Q = \frac{Q}{\rho n^2 D^5} \quad (3)$$

$$\eta_O = \frac{J K_T}{2\pi K_Q} \quad (4)$$

Here,  $V_A$  is the speed of the inflow,  $n$  is the rps of the propeller,  $D$  is the diameter of the propeller, and  $\rho$  is the density.

### 2.3. Reversed POW Test

The POW test described in Section 2.2 is performed under open water condition that the inflow is not affected by the surrounding environment to measure the propeller characteristic only. In this case, the towing direction of the carriage is determined so that the inflow to the propeller is uniformly formed without being affected by the shaft as shown in Figure 3a. However, open water condition cannot be applied to test for estimating PBCF performance. The reason is that the PBCF affects the hub vortex generated in the wake of the propeller as shown in Figure 2. However, in a general POW test, the hub vortex is not generated since the shaft is located in the wake of the propeller.

As shown in Figure 3b, to estimate the performance of the PBCF, the carriage must be towed to reverse direction of the general POW test, which is called a reversed POW (rPOW) test. However, the rPOW has a disadvantage in that the POW performance is estimated on non-uniform inflow disturbed by the shaft and carriage.

To compensate for these issues and to estimate the open water performance of a propeller equipped with PBCF using the rPOW, this study used the correction method described in below.

Firstly, POW and rPOW tests were respectively conducted for the propeller without PBCF as shown in Figure 3a,b. Secondly, absolute differences ( $K'_T, K'_Q$ ) between  $K_T$  and  $K_Q$  measured in the two tests were obtained. These values were assumed to be the difference in the uniformity of the inflowing flow. As shown in Figure 3d, the rPOW test was also conducted for the propeller with PBCF. Now, by adding  $K'_T$  and  $K'_Q$  to the rPOW result, the difference between non-uniform and uniform flow can be corrected. Finally, open water performance of the propeller equipped with PBCF could be obtained as shown in Figure 3c.

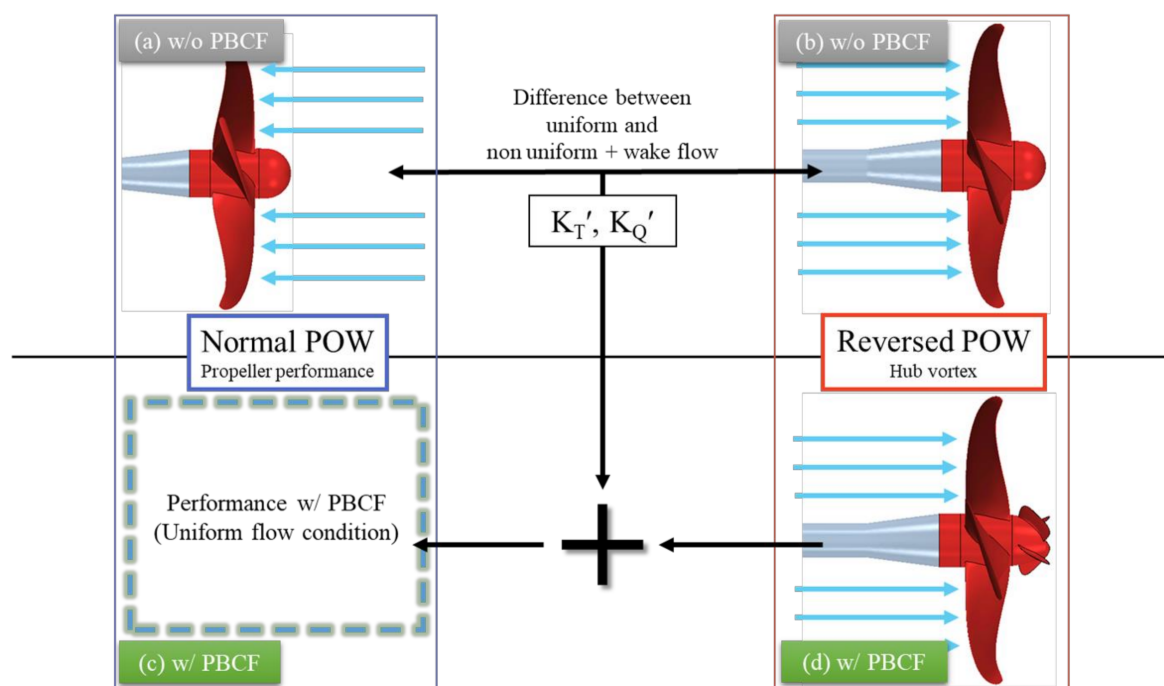


**Figure 3.** Procedure for estimation of POW performance with PBCF.

### 2.4. Self-Propulsion Test

The self-propulsion test is performed for estimating the propulsion performance of a propeller when a ship system goes forward at the target speed by the propeller's propulsion force. From this, the overall performance and various efficiencies of the designed hull-propeller system are estimated. The most important purpose in the self-propulsion test is to find the propeller rps at the self-propulsion point (SPP) or the self-propulsion condition

in which the resultant force of the system is zero as the propeller's thrust and the hull's resistance are equal. Self-propulsion condition means that the system is cruising only by the thrust of the propeller during towing the model ship at a specific ship speed.

Physical quantities that are directly measured in a self-propulsion test include the propeller thrust, the propeller torque, and the resultant force of the system at various rps of the propeller with a specific ship speed. By analyzing these data, the propeller performance under the self-propulsion condition is found. By combining results of self-propulsion test with bare resistance and POW curve obtained in Sections 2.2 and 2.3, the ITTC 1978 self-propulsion analysis is performed. Final results of the ITTC 1978 self-propulsion analysis include the self-propulsion coefficients, such as the BHP ( $P_B$ ), DHP ( $P_D$ ) at full-scale, various efficiencies of the system, the wake fraction ( $w$ ), the thrust deduction factor ( $t$ ), and so on. In this paper, DHP was considered as 98% of BHP. The efficiency includes the propeller open water efficiency ( $\eta_O$ ), the relative rotative efficiency ( $\eta_R$ ), the behind hull efficiency ( $\eta_B$ ), the hull efficiency ( $\eta_H$ ), and the quasi-propulsive efficiency ( $\eta_D$ ). This paper only included results of the ITCC 1978 method. The ITTC [15] may be referred to for detailed explanations of each efficiency, each coefficient, and the process of the ITTC 1978 analysis method.

## 2.5. Numerical Modeling

### 2.5.1. Governing Equations

To obtain the average performance on the engineering sense, the ensemble-averaged incompressible RANS (Reynolds-Averaged Navier–Stokes) Equation (5), and the continuity Equation (6) were used as the governing equation.

$$\frac{\partial \bar{u}_i}{\partial t} + \bar{u}_j \frac{\partial \bar{u}_i}{\partial x_j} = -\frac{1}{\rho} \frac{\partial \bar{p}}{\partial x_i} + \frac{\partial}{\partial x_j} \left[ \nu \left( \frac{\partial \bar{u}_i}{\partial x_j} + \frac{\partial \bar{u}_j}{\partial x_i} \right) - \overline{u'_i u'_j} \right] + g_i \quad (5)$$

$$\frac{\partial \bar{u}_j}{\partial x_j} = 0 \quad (6)$$

where,  $u$  is the velocity,  $x$  is the position,  $t$  is the time,  $p$  is the pressure,  $\nu$  is the kinematic viscosity,  $g$  is the gravitational acceleration, and  $\overline{u'_i u'_j}$  is the Reynolds stress (turbulence stress).

Although Carrica et al. [16] have announced that, in a self-propulsion test, DES (Detached Eddy Simulation) yields similar results to experiments with the RANS equation, the DES equation takes a long time to calculate with too many grids for engineering purposes. For this reason, most previous studies on the self-propulsion analysis [17–24] have used the RANS equation.

In this study, CFD simulations for resistance, POW test, and self-propulsion test were sequentially performed. At first, in the simulation of the resistance test, numerical modeling and the grid system for analysis of the flow field around the hull were verified. This was performed by comparing and verifying results of model tests performed under the same environmental condition. Next, in the POW simulation, the numerical modeling and the grid system for analysis of the rotational flow around the propeller were verified. Finally, self-propulsion simulation was performed by simply combining two grid systems that had already been verified with same numerical modeling of other simulations. The physical quantity of the flow field between two grid systems was exchanged by the interface.

### 2.5.2. Turbulence Model

It is widely known that laminar flow exists at the non-negligible ratio on the propeller surface at the model-scale with the laminar-turbulent transition phenomenon [25–28]. With recently continuous development of numerical models, some numerical models capable of implementing laminar-turbulent transition are being developed and various studies [29–34] have applied the transition model to the model-scale propeller analysis. In most studies, when the transition model is applied, analysis results are similar to results of

experiments. Therefore, in this study, for analyses including the model-scale propellers in POW and self-propulsion tests, a turbulence modeling was constructed by combining the  $\gamma$ - $Re_{\theta}$  transition model [35,36] with the SST (Shear Stress Transport)  $k$ - $\omega$  turbulence model. Although various turbulence models from the  $k$ - $\epsilon$  model and the  $k$ - $\omega$  model are widely used for analyzing engineering problems [37], the others were not considered in this study since the  $\gamma$ - $Re_{\theta}$  transition model could only be combined with the SST  $k$ - $\omega$  model.

Due to the complexity of the numerical model and the characteristics of transition point prediction by measuring the turbulence intensity outside the boundary layer, the  $\gamma$ - $Re_{\theta}$  transition model might cause many numerical errors in simulations involving the free surface in which the phase of matter and the boundary layer might change continuously. Therefore, in this paper, the  $\gamma$ - $Re_{\theta}$  transition was applied only in the POW test that did not include free surface and the  $\gamma$  transition model which has a simplified transition point prediction mechanism was used in resistance and self-propulsion tests that included free surface. This simplified application might degrade the accuracy of the laminar-turbulent transition prediction. However, Kim et al. [34] have shown that the most laminar-turbulence transition on the surface of the model propeller is bypass transition by the strong turbulence intensity around the propeller tip vortex, not delicate natural transition with the development of the boundary layer. So, the uncertainty in transition point prediction due to simplified model is not expected to significantly undermine the reliability of simulations.

To consider the viscous sublayer, the grid near the wall was configured so that the wall  $y^+$  was less than 1. The boundary layer was solved directly by the governing equation not using the wall function. These are known to be necessary when using the transition model [35].

### 2.5.3. Grid Systems and Numerical Modeling

Star-CCM+ ver. 11.06.010, a commercial CFD software, was used for generating grids and analyzing the flow field. In POW and self-propulsion analysis, the rotation of the propeller was implemented using the sliding mesh method. Although Shen et al. [38] have obtained similar results to the experiment by implementing the propeller rotation using an overset mesh, the difference from the sliding mesh method was not significant. Since the overset mesh method required relatively large computational resources, the sliding mesh method was applied to POW and self-propulsion analysis in most previous studies.

All simulations were performed on a model-scale to obtain sufficient effectiveness in reproducing real situations using simulations. Recently, the full-scale simulation for the self-propulsion test has been actively studied like Ponkratov and Zegos [39], Wang et al. [40], Jasak et al. [41], and so on. However, the verification and validation method for full-scale simulation remains unclear, making it difficult to secure the reliability.

For a grid system, a hexahedral mesh, in which the static region around the hull without motion which had a cube shape, was used. This was because the hull had a relatively simple shape compared with the propeller and a hexahedral mesh had a structural shape and arrangement that would be advantageous for expressing the free surface. For the rotating region around the propeller, a polyhedral mesh was used to reproduce the complex shape of the propeller. In the POW test and self-propulsion analysis, the connection between the two regions was configured using the internal interface of Star-CCM+ (Figure 4).

The free surface was implemented by Eulerian multiphase and VOF (Volume of Fluid) model [42]. The 2nd-order of (High-Resolution Interface Capturing) scheme [43] was used to track the shape of the free surface. In addition, VOF damping regions were set around side boundaries to offset reflected waves caused by hull-induced waves. The numerical modeling methods used in the simulations are summarized in Table 1.

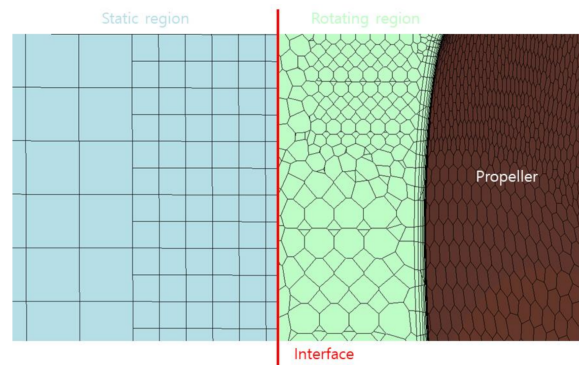


**Figure 4.** Grids systems around interface between static and rotating regions.

**Table 1.** Numerical modeling.

Test	Resistance	POW	Self-Propulsion
Governing equations		Incompressible RANS and continuity equations	
Scheme		3rd order MUSCL (spatial) 2nd order implicit unsteady (temporal)	
Turbulent model		SST k- $\omega$ model	
Wall treatment		Low y+ wall treatment (wall y + 1 < 1)	
Transition model	$\gamma$	$\gamma$ -Re $_{\theta}$	$\gamma$
Free surface	Eulerian multiphase and VOF	N/A	Eulerian multiphase and VOF
Grid	Hexahedral	Hexahedral (static region) Polyhedral (rotating region)	

### 3. Resistance Test

#### 3.1. Simulation Condition

The target ship was a 176K bulk carrier (hereinafter, referred to as 176K) with the rudder. Its shape is shown in Figure 5a and specifications are listed in Table 2. The draft was set to the full load condition with the even trim. The speed range was set to be 9–15 knots as in the model test. The Froude number (Fn) was 0.08–0.15 and the Reynolds number (Re) was in the range of  $6.18 \times 10^6$ – $1.03 \times 10^7$ . Time-step was automatically adjusted so that the Courant number (Cn) did not exceed 1 to minimize the variation of the numerical model according to the change in speed.

**Table 2.** Dimensions of the 176K bulk carrier (design draft, full-scale).

Configuration	Symbol (Unit)	Value
Scale ratio	$\lambda$	32.6
Length between perpendicular	L <sub>pp</sub> (m)	282.0
Breadth	B (m)	45.0
Draft	T (m)	18.3

Figure 5b shows the numerical towing tank and boundary conditions. The hull was analyzed for both port and starboard side considering the self-propulsion test. For boundary conditions, the flow velocity and the pressure gradient were set by the velocity inlet and pressure outlet. The slip wall was applied to all other outsides.

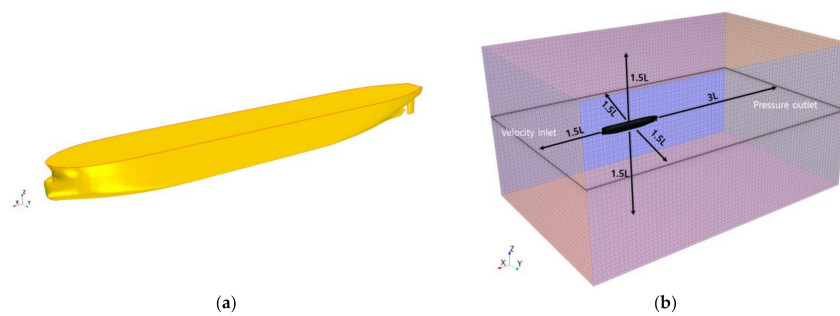


**Figure 5.** Geometrical configuration of the simulation for the resistance test: (a) The geometry of the 176K bulk carrier and (b) numerical towing tank with boundary conditions.

Figure 6a shows the snapshot of the grid system in the middle longitudinal-sectional plane of the hull. The grid resolution was highly concentrated in the vicinity of the stern, the bow, and the free surface. A convergence test was performed to estimate the effectiveness of the grid system around the hull without free surface. By increasing the size of all cells to the square root of 2, five grid systems (G0: 1,261,198; G1: 2,552,240; G2: 5,244,354; G3: 10,716,412, and G4: 27,540,510) were generated. Estimated total resistances for each grid system are shown in Figure 6b. Here,  $x$  axis refers to the grid index. Left axis and bar graph refer to the estimated resistance. Right axis and line refer to the rate of difference between result of G4 and measured value. A rapid change was observed between G1 and G2. After that, the value changed in the range of 0.5% compared to the G4 result. Even in G4, the grid system was not fully converged. In this study, to obtain appropriate accuracy and economic computation efficiency from an engineering sense, the G2 grid system was used. Since the number of grids increased rapidly from G3, the change between G2 and G4 was relatively small. The final number of the G2 grid system was about 6,700,000 including the grid refinement around the free surface.

To investigate the numerical uncertainty of the simulation using G2 grid system, the GCI (Grid Convergence Index) was calculated through G1–G3 grid systems. GCI is an index proposed by Roache [44] to evaluate grid convergence and predict the convergence solution through the Richardson extrapolation method. As the result, GCI23 was calculated as 0.13%. Also, the difference between the predicted convergence solution obtained through the results of G1–G3 grid system and the total resistance from G4 grid system is in a very small range of 0.27%. Therefore, assuming the limit of the number of grids that can be used realistically is G4, a numerical uncertainty of the order of 0.4% is expected in the resistance simulation when using the G2 grid system.

The computation time spent per each ship speed was about 100 h using an 8-core Intel I7-5960 CPU.

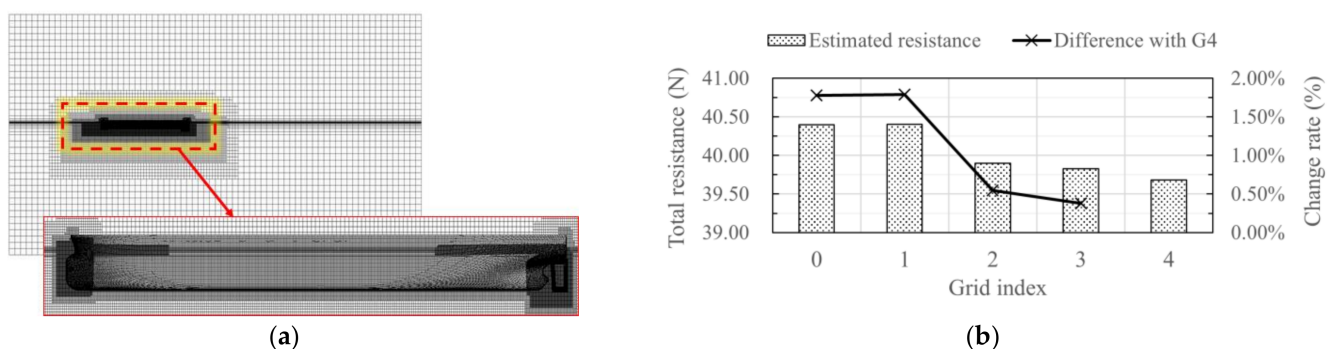


**Figure 6.** Information of the grid system for the resistance test: (a) side view of the grid system and (b) results of the grid convergence test.

### 3.2. Simulation Results and Verification

Figure 7a shows results of estimating the total resistance coefficient ( $C_T$ ) for each speed.  $C_T$  is the dimensionless quantity of  $R_T$  and the subscript M meant the model-scale. Here, the solid line and the mark indicated the estimated simulation value and the experimental value, respectively. These values are indicated on the left axis. The dotted line and the right axis indicate the relative error of the simulation with the experiment. Here, the maximum relative error was 1.2%.

Figure 7b shows the estimated result of the nominal wake distribution compared with the experiment result. Here, the red solid line represents the experiment value and the blue solid line represents the estimated value from the simulation. The wake distribution represents the value obtained by dividing the flow velocity by the ship speed at each point. In the experiment, the wake distribution was measured through a pitot tube installed at the rudder position. It displays with a contour between 0.1 and 0.9 from the inside to the outside. The nominal wake distribution represents inflow to the propeller, which makes a great influence on the accuracy of the propulsion performance estimation in the self-propulsion test. Wake distributions showed similar trends between experiments and simulations. However, there was a slight difference near the boss which was the center of the circle. But the propeller's propulsion power was small near the boss due to the low flow velocity. Thus, the influence of this error to the propulsion performance estimation was not so large.

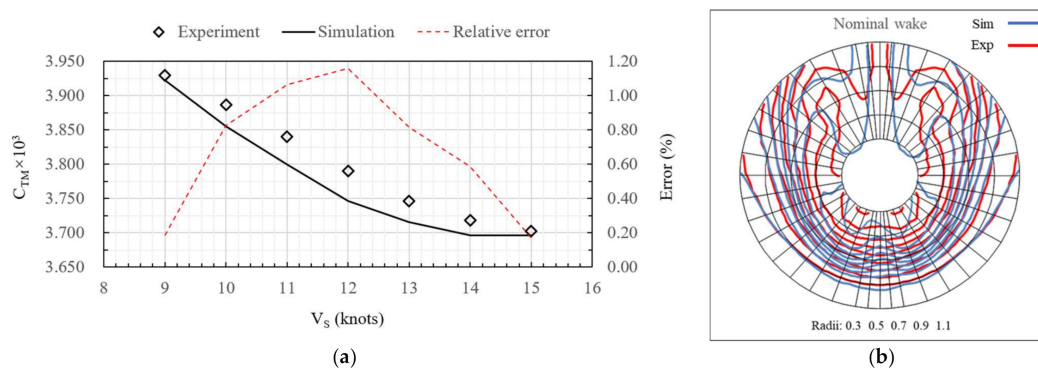


**Figure 7.** Estimated results of the resistance test compared with the experiment: (a) total resistance coefficient and (b) nominal wake distribution.

## 4. POW Test

### 4.1. Simulation Condition

Figure 8a shows the target propeller of the 176K with PBCF. The scale ratio of the propeller is 32.6, the same as that of the hull. The diameter at the full-scale is 8.15 m. With a fixed rps at 17, the advance ratio was changed from 0.1 to 0.75, the same as in the experiment. At this time, the representative Reynolds number at 70% radius of the propeller was  $6.79\text{--}7.21 \times 10^5$ . The simulation was performed under conditions shown in Figure 3a,b,d. Performance comparison with the experiment for validation of the simulation was carried out under conditions shown in Figure 3a.

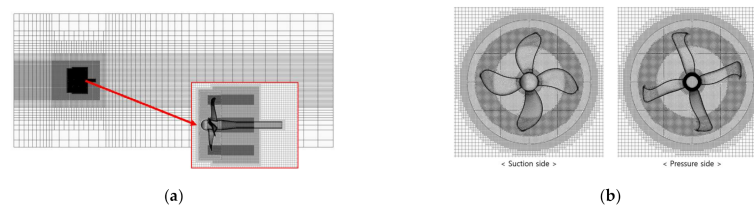
Figure 8b shows the size and boundary conditions of the numerical tank used in the POW test. The numerical tank was composed of a rotating region included the propeller where the domain rotated and a static region that was an external environment. As for the boundary condition, similar to the resistance test, the flow velocity and the pressure gradient were calculated based on the velocity inlet and the pressure outlet. Other side boundaries were set as the slip-wall.

Figure 9a,b shows the snapshot of the grid system in the longitude-sectional plane and the transverse-sectional plane, respectively. The high-resolution grid was generated to concentrate only near the propeller structure in the entire computational domain. In particular, the grid refinements were adopted near the tip and hub of the propeller blade,

where vortex generation is expected. Also, these refinement regions were extended toward the propeller wake for sufficient transport of the tip and hub vortices.



**Figure 8.** Geometrical configuration of the simulation for the POW test: (a) the geometry of the propeller with PBCF and (b) numerical towing tank with boundary conditions.



**Figure 9.** Snapshots of the grid system for the POW test: (a) side view and (b) front and rear view.

To conduct the grid convergence test, five grid systems were generated for the rotating region (G0: 720,895; G1: 1,422,222; G2: 4,063,483; G3: 7,164,420; and G4: 17,724,697). Results are shown in Figure 10a. Here, the x axis represents the number of grids. The left axis and dotted line represent  $K_T$ . The right axis and solid line represent the prediction result for  $10K_Q$ . As for  $10K_Q$ , there was a large variation in G0–G1. It was within the convergence range by maintaining relatively small changes in G2. On the other hand,  $K_T$  showed convergence at the high resolution after the G3 with a large variation at G0–G3. This was related with the resolution change near the propeller tip. This could be confirmed indirectly from the distribution of the mean tangential velocity for each radius shown in Figure 10b. In this study, in order to maintain the engineering sense as in the resistance test, the G2 grid system was finally used by compromising some analysis accuracy of the tip vortex. At this time, the grid number was set at about 4 million in the rotating region and 6 million in the static region for a total of 10 million. The reason why the static region had a higher grid number was the grid refinement near the tip and hub for minimize numerical errors due to development of the tip and hub vortex as shown in Figure 9a.

The GCI was calculated through G2–G4 grid systems to investigate the numerical uncertainty of the G2 grid system, and the GC23 for  $K_T$  was calculated as 0.94%. Therefore, when considering the G4 grid system as the limitation of the computational resources, the numerical uncertainty for  $K_T$  becomes 0.94%. In the case of  $K_Q$ , the GCI could not be calculated because the trend of estimated  $K_Q$  with the number of grids did not show any convergence, and it was difficult to determine the numerical uncertainty about  $K_Q$ . For that reason, it is desirable to investigate the accuracy on predicting  $K_Q$  only through direct comparison with experimental results.

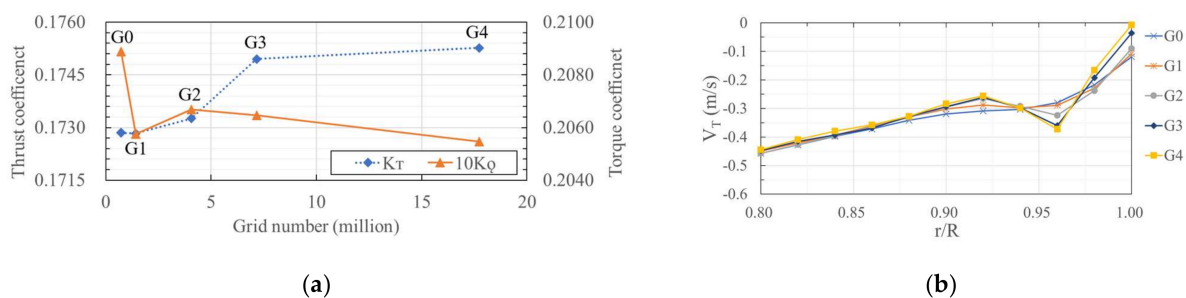
Figure 11a shows estimation results of  $K_T$  and  $10K_Q$  according to time-step in the grid system of G2 together with the rotational angle of the propeller per time-step. When the time-step was 0.001–0.0005 s, results almost converged, in which the rotational angle per time-step was about 3 degrees. For reference, ITTC [45] recommends the rotational angle per time-step to be set at 0.5–2 degrees when estimating the propeller performance using the CFD simulation. Similar results were obtained in this study. However, as shown in Figure 11b, there was no significant difference in the mean tangential velocity at each propeller radius according to the time-step, which showed the same trend for radial and axial velocities. This means that the variation of the mean flow field according to time-step is small. Figure 12 illustrates vorticity distribution around the propeller. It showed large variations of the flow continuity around the interface between two time-step. Thus,

such difference in propeller performance estimation according to time-step was mainly caused by the motion processing rather than the accuracy of the flow estimation. Therefore, for engineering purposes, in this paper, the time-step was set at 0.01 s which showed a difference of 0.5% from the converged result in the POW test. However, in the self-propulsion test in which the interaction between hull/rudder and the propeller wake at each time-step was important, the time-step was set at 0.001 s. The computation time spent per each ship speed was about 20 h using an 8-core Intel I7-5960 CPU.

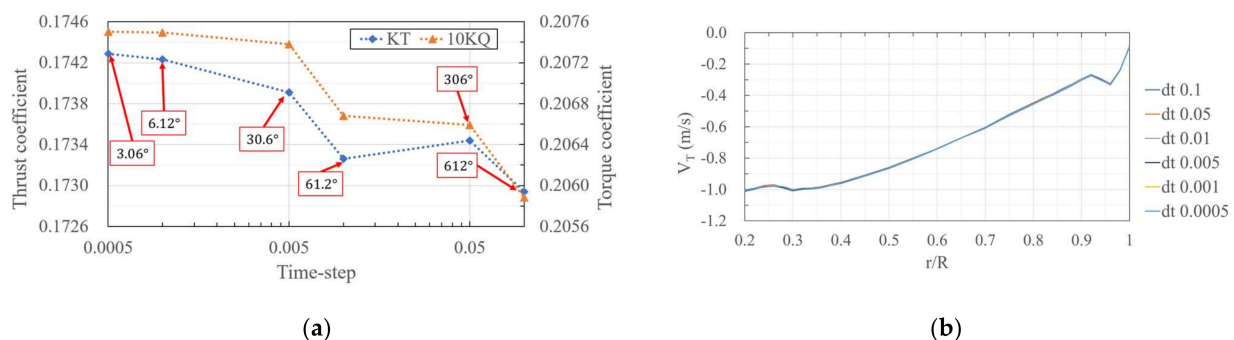
#### 4.2. Simulation Results and PBCF Efficiency Analysis

Figure 13a shows the propeller performance for each advance ratio without PBCF. Here, the solid line indicates estimated values from the simulation and markers indicate the experimental value. From top to bottom,  $\eta_O$ ,  $K_T$  and  $10K_Q$  were plotted. On the graph, the difference between simulation and the experimental results were small that qualitative comparison was difficult. At an advance ratio of 0.6 or less, the average relative error was about 1% and the maximum error level was about 2%. However, at an advance ratio of 0.7, a large error of more than 4% was found. Since the propeller's operational advance ratio at the self-propulsion point was 0.4–0.45, this error level would have little effect on the self-propulsion performance estimation.

Figure 13b shows change rates of the propeller performance by PBCF in the experiment and the simulation. Here, the dark bar represents the experimental value and the light bar represents the simulation estimated value. Values about  $K_T$ ,  $10K_Q$ , and  $\eta_O$  are displayed from left to right for each advance ratio, corresponding to the difference in performance between two test conditions in Figure 3a,d. At first,  $K_T$  increased at most advance ratio due to PBCF. Increasing rate was about 5% in the experiment and by about 0.4% in the simulation on average. For  $10K_Q$ , it was decreased by about 0.4% on average in both the experiment and the simulation due to PBCF. Consequently, due to an increase of  $K_T$  and a decrease of  $10K_Q$ ,  $\eta_O$  increased (1% on average in the experiment and 0.7% on the average in the simulation).



**Figure 10.** Results of the grid convergence test in the POW test: (a)  $K_T$  and  $10K_Q$  and (b) radial distribution of circumferential mean tangential velocity.



**Figure 11.** Results of time-step convergence test in the POW test: (a)  $K_T$  and  $10K_Q$  and (b) radial distribution of circumferential mean tangential velocity.

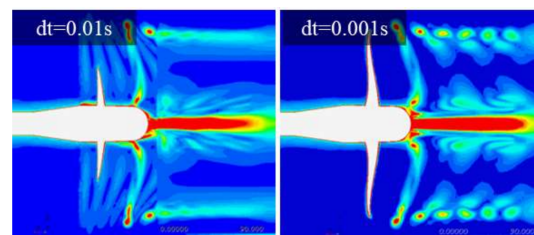


Figure 12. Vorticity near the propeller according to time-step.

Although change rates of the propeller performance due to PBCF in the experiment and the simulation were not exactly the same, their ranges and average values were similar. And these are consistent with results of a previous study [8] showing an increase in thrust and a decrease in torque with PBCF. As mentioned in the introduction, the quantitative value of efficiency gain by PBCF under POW condition was different among previous studies. However, results of the present study had above average reliability among studies because trend of the simulation results was consistent with the experiment.

As described in Section 4.1, the time-step was set at 0.01s for the POW simulation, which may cause a difference of less than 0.5% from the analysis using the converged time step. Therefore, it would be said that there was a numerical uncertainty of a 0.5% level in each simulation case. This means that the numerical error can be misunderstood as the effect of PBCF (0–1.0%). However, since the trend of change in propeller performance due to PBCF was similar in the experiment and simulation, it does not seem that the numerical uncertainty dominantly affects the estimation of the relative change in performance by PBCF.

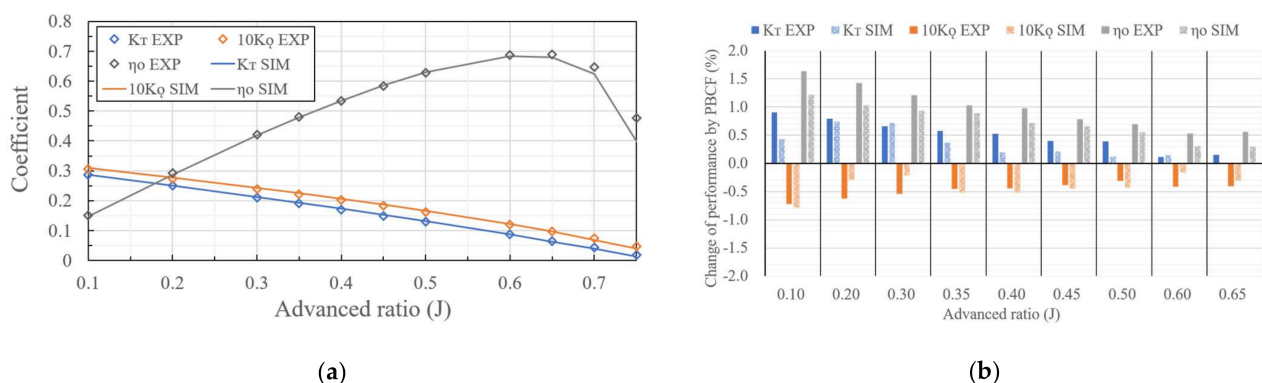
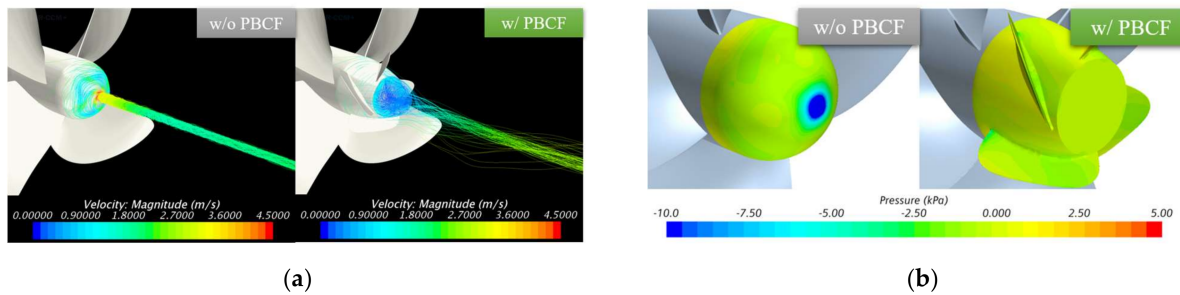


Figure 13. Estimated results of the POW test compared with the experiment: (a) propeller performance without PBCF and (b) change rates of propeller performance by PBCF.

Figure 14a shows simulation results for streamlines of the hub vortex with and without PBCF. The hub vortex that was strongly developed by gathering of the flow at the end of the boss cap was broken due to the PBCF. This was because the tip of the PBCF had the shape of a divergence cap so that it could forcibly separate the flow. The corresponding pressure field is shown in Figure 14b. It was recognized that the strong negative pressure due to rotating momentum of the hub vortex was suppressed by the PBCF. This effect contributed to increase the thrust of the propeller because the extinction of the negative pressure located in the wake direction reduce drag of the structure.

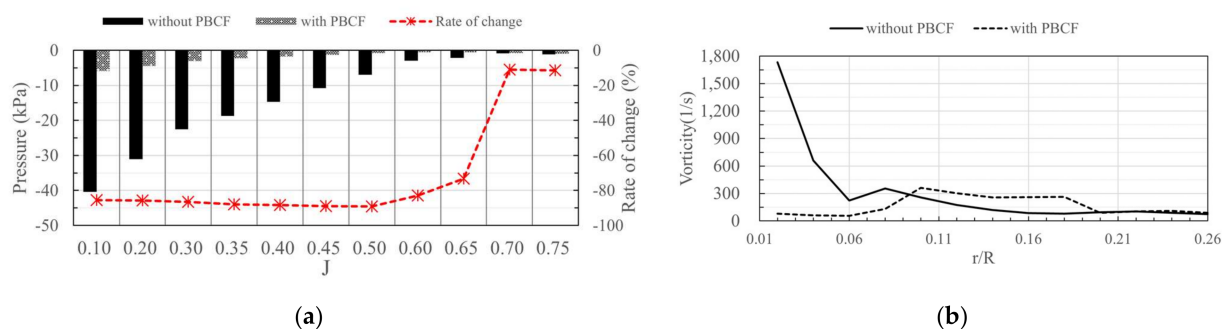


**Figure 14.** Visualized variation of flow field by PBCF in the POW simulation: (a) streamlines of the propeller hub vortex and (b) pressure distribution on the boss cap and PBCF.

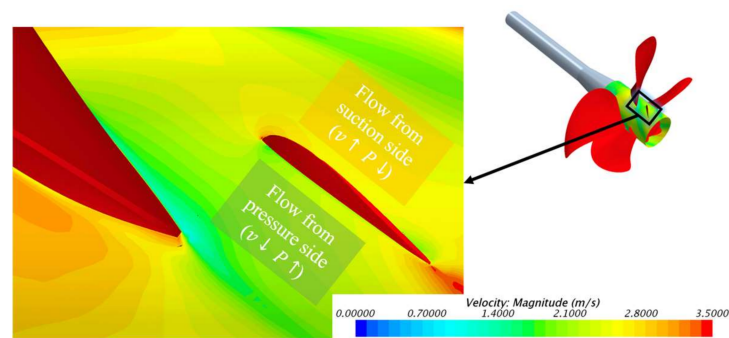
Figure 15a shows the minimum pressure on the boss cap with and without PBCF according to advance ratio. Here, the left axis and the bar graph represent the pressure and the right axis and the dotted line represent the change rate of the minimum pressure by PBCF. It was confirmed that the absolute value of the minimum pressure on the boss cap decreased by about 90% due to PBCF. Furthermore, it was confirmed that the average pressure acting on the entire surface of the boss cap decreased by 50% or more due to PBCF.

Figure 15b shows the mean vorticity of each propeller radius at the wake flow near the boss cap. Here, the dotted line represents the estimated value with PBCF and the solid line represents the estimated value without PBCF. It was confirmed that the maximum value of vorticity at the rear end of the boss cap was significantly lowered due to PBCF. Meanwhile, the vorticity slightly increased in the range of  $r/R = 0.1$ – $0.2$  when PBCF was installed. Interestingly, the total vorticity was about 150/s regardless of the installation of PBCF when integrating the graph. From this, it could be understood that the PBCF operates by simply blocking the flow interaction from the shape of the cap with maintaining the kinetic energy of strong rotation flow from the trailing edge.

Figure 16 shows velocity distribution in the  $0.2 r/R$  plane around overall the propeller structure. It was confirmed that the flow with low velocity and high pressure from the pressure side flowed along the left side of the PBCF fin. Meanwhile, the flow with high velocity and low pressure flowed along the right side of the PBCF fin. As a result, the net force was generated by the pressure difference between both sides of the PBCF fin. This force could be induced in the same direction as rotating direction of the propeller when the fins were properly arranged. This meant that, the propeller had additional rotating force by PBCF fins so that the torque of the propeller was decreased.



**Figure 15.** Variation of flow field by PBCF: (a) minimum pressure acting on the boss cap and PBCF as a function according to the advance ratio and (b) radial distribution of circumferential mean vorticity at the wake of propeller.



**Figure 16.** Velocity contour on 0.2 r/R plane near fins of the PBCF and propeller blade.

## 5. Self-Propulsion Test

### 5.1. Simulation Condition

Figure 17a shows the geometry of the 176K with the propeller. Specifications of the hull and the propeller are the same as those mentioned above. Simulations for the self-propulsion test were performed only at the lowest speed of 9 knots, the design speed of 12 knots, and the highest speed of 15 knots in a velocity range of the model test considering a long simulation time of the self-propulsion test. At each speed, the simulation was performed with selecting two rps around the self-propulsion point obtained in the model test. From this result, the self-propulsion point in the simulation was estimated with the theoretical towing force. Moreover, ITTC 1978 analysis was performed with the total resistance and the POW curve obtained from simulations of the resistance and the POW test. From this, the self-propulsion coefficient, the efficiency, and the BHP at full-scale were derived. All tests in the simulation and the experiment were performed both with and without PBCF for estimating the efficiency of PBCF in the self-propulsion condition.

The numerical tank and the grid system were configured in the same way as those described in the resistance test and the POW test. As shown in Figure 17b, the rotating region used in the POW test was transited into the propeller position. Finally, a total of 11 million grids were used with about 4 million in the rotating region and about 7 million in the static region. Time-step was set to be 0.001 s as mentioned in Section 4.1. An 84-core parallel computing server configured with an Intel Xeon E5-2690 CPU was used for the self-propulsion simulation, with approximately 170 h of computation time rps.

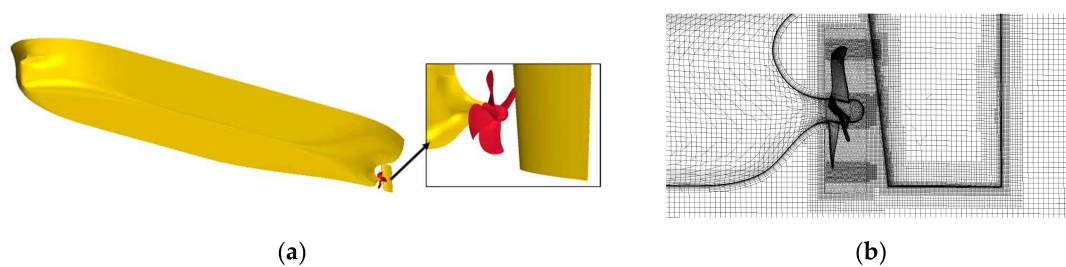


**Figure 17.** Configurations of the simulation for the self-propulsion test: (a) the geometry of the hull with the propeller and (b) grid system near the propeller.

### 5.2. Simulation Results and Verification

At first, simulation results without PBCF were compared with experiment for validation of the simulation. Figure 18a shows relative errors between simulation and experiment results of the propulsion performance at self-propulsion point of three ship speeds. The difference was less than 2% for thrust and rps. However, estimated torque was 3% higher than that in the experiment. However, not all of these large differences in torque between the experiment and simulation can be considered only as simulation errors. Especially, it

seems to be very difficult to obtain reliable measurements even in experiments with too small a range, where the absolute value of the torque is less than 1.5 N m.

Figure 18b shows relative errors between simulation and experiment for self-propulsion factors at each ship speed. The relative errors of  $\eta_B$  and  $\eta_D$  directly related with the torque in Figure 18a during the ITTC 1978 analysis were more than 3% which was bigger than other efficiencies. On the other hand, the self-propulsion coefficient related to the total resistance, rps, and thrust showed a low relative error under 2%. For reference, although not included in this paper, the thrust deduction factor, the thrust, and the rps of the full-scale showed relative errors of less than 2%. However,  $P_B$  showed an error range of 2–5% because the BHP is related to the torque also.

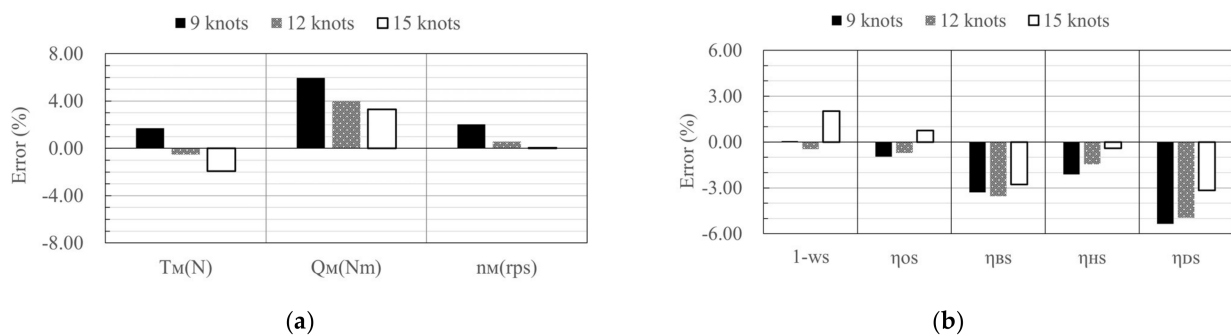


**Figure 18.** Relative errors of simulation results with the experiment in the self-propulsion test: (a) propulsion performance at the self-propulsion point and (b) self-propulsion factors.

Figure 19 shows rates of change of the propulsion performance by PBCF at each ship speed in simulation when the propeller kept rotating at fixed rps, not the self-propulsion point. Specifically, the quantitative rate of change for each performance did not vary greatly depending on the ship speed. The thrust was increased by about 1% while the torque was decreased by about 0.5%, resulting in an increase of about 1.5% for the propeller efficiency by PBCF installation. Here, it was confirmed that the trend of thrust increase and the torque decrease due to PBCF were the same under both POW and self-propulsion conditions. However, the increased rate of the thrust and the propeller efficiency was 0.5% higher at the self-propulsion condition than the POW condition. However, although the effect of PBCF under the self-propulsion condition was improved over that under the POW condition, it was still lower than the performance of PBCF of 3–10% measured from full-scale measurement and sea-trial as described in the introduction.

Figure 20 shows rates of changes of the propulsion performances by PBCF at the self-propulsion point of each ship speed. Firstly, in the simulation, as shown in Figure 20a, the rps of the self-propulsion point was decreased by 0.4% on average. This directly confirmed that the propeller thrust was increased at a specific rps due to PBCF so that the rps of the propeller for providing a thrust equal to the resistance acting on the ship system was reduced. Meanwhile, as the rps was decreased, the torque which was a frictional force of the propeller was also decreased. Adding the torque reduction effect of the PBCF, the torque of the self-propulsion point was finally decreased by about 1.5%. This is a very positive result considering that the energy used to rotate the propeller is derived from the rotational speed and the torque. On the other hand, as shown in Figure 20b, the rates of change of the propulsion performances by PBCF in the experiment did not show a consistent trend depending on the ship speed. Since PBCF showed a relatively consistent effect according to the advance ratio in the model test under POW condition, it was hard to accept the experimental results in this self-propulsion test. In addition, when the thrust generated by the propeller was increased at a specific rps due to PBCF as in the POW test, the PBCF effect should only cause a decrease of the rps at the self-propulsion point, assuming that the increase of hull resistance due to PBCF was small. However, the thrust of the self-propulsion point increased after installing the PBCF in the experiment. This means

that the PBCF led to an increase in hull resistance. However, the finding that a small ESD installed at the end of the propeller increased the hull resistance was somewhat contrary to common sense. Thus, considering the consistency of measured values, it was found that the quantitative value and the trend of the improvement due to PBCF were more reliable in the simulation than in the experiment. Since the self-propulsion test was carried out repeatedly in the same towing tank, the environmental condition around the model ship can continuously change in the experiment. It was hard to consistently measure small performance changes of 0.5–1.5% due to PBCF within the error range of the experiment. However, in the experimental results, it was clearly shown that the propulsion performance at the self-propulsion point was changed in a positive direction by PBCF with an increase in the thrust and the decrease of rps and torque.

Figure 21a shows vorticity around the propeller in the simulation. Here, after installing the PBCF, the vorticity at the center of the boss cap was greatly reduced. In addition, as shown in Figure 21b, a strong negative pressure generated at the center of boss cap disappeared with PBCF. These variations of flow field by PBCF which shows the mechanism of PBCF was the same as that of the POW condition.

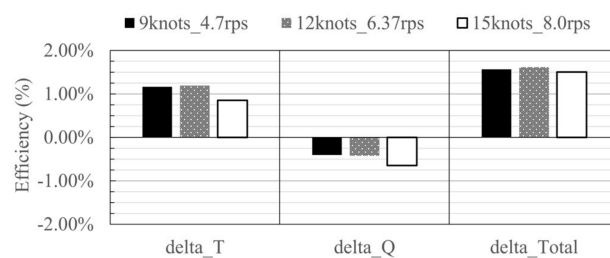


Figure 19. Variations of the propulsion performance by PBCF in the self-propulsion simulation.

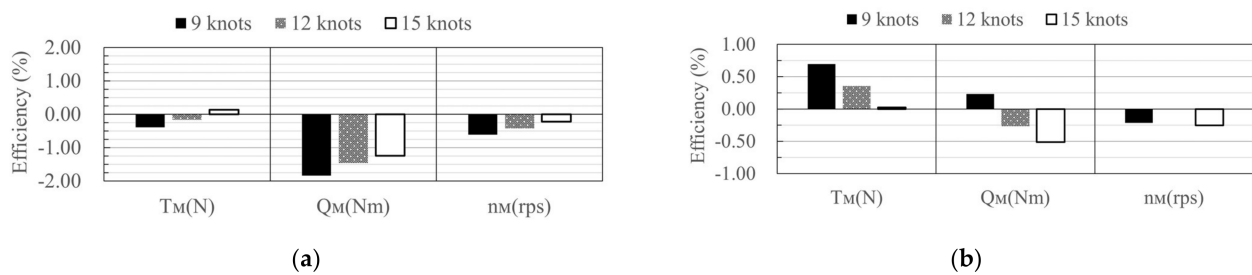


Figure 20. Effect of PBCF on the propulsion performance at the self-propulsion point: (a) simulation and (b) experiment.

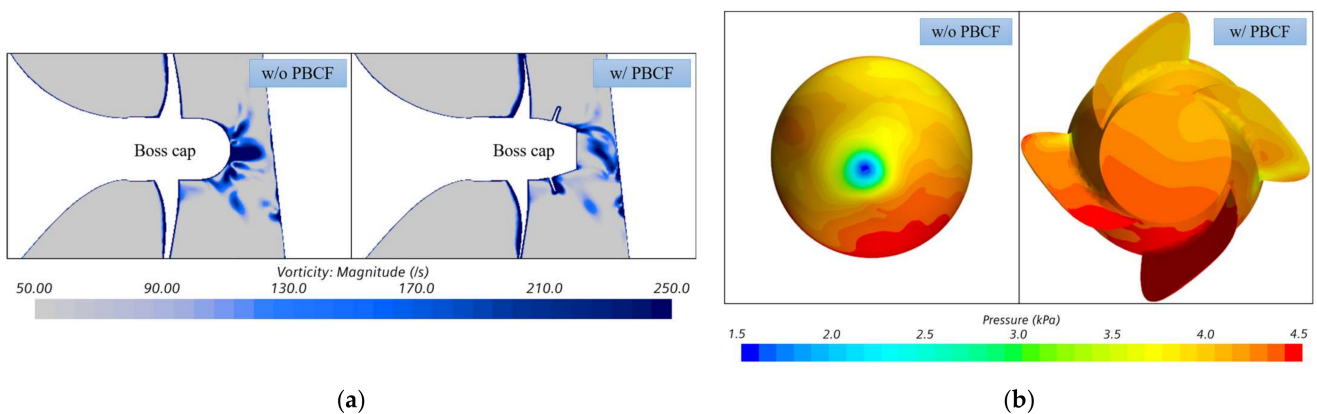


Figure 21. Visualized variation of flow field by PBCF in the self-propulsion simulation: (a) vorticity near the propeller and (b) pressure distribution on the cap or PBCF.

Figure 22 shows rates of change of full-scale self-propulsion factors due to PBCF at each ship speed. In simulation, as shown in Figure 22a, the changes by PBCF were relatively consistent according to ship speed like results in Figure 20a. In addition, torque reduction of about 1.5% at the self-propulsion point caused 1.5% reduction in  $\eta_B$  and  $\eta_D$ . On the contrary, in the experiment, since the changes of the propulsion performance by PBCF at the self-propulsion point was inconsistent according to ship speed, the changes in self-propulsion efficiency were not completely consistent also. Nonetheless, most of self-propulsion efficiencies increased except for that at 9 knots by PBCF in experiment. However, the large difference of the wake coefficient in the experiment indicated some instability of the experiment. This was because the flow change in front of the propeller by PBCF was not obvious from a common sense. One important feature was that changes of propeller open water efficiency by PBCF in both the experiment and simulation were very similar, showing an average of 0.7%. This rate of change of  $\eta_O$  was also similar to results of the POW test.

Figure 23 shows rates of change of the propulsion performance and BHP by PBCF at full-scale both in the simulation and experiment. Consequently, reduction rates of the BHP were about 1.5% and 0.5% on average in the simulation and the experiment, respectively. Here, estimated PBCF efficiency of 0.5–1.0% under the POW condition had a similar range to the reduction of BHP in the self-propulsion test. Therefore, the POW test also can provide somewhat valid results for performance evaluation of the PBCF.

As described above, the PBCF performance estimated from the self-propulsion test in this paper was largely different from the performance of 3–10% obtained from full-scale measurement. However, Katayama et al. [11] have analyzed Fuel Oil Consumption (FOC) by month and found that change of efficiencies by PBCF per month show remarkable variations, meanwhile the ship with PBCF shows 1–2% reduction in DHP at a specific month (for example, November and December) as shown in Figure 24. Thus, it is hard to say that results of the present study are completely unreliable. In addition, in the full-scale measurement, a high reduction amount of 7% in DHP was observed, making it difficult to evaluate the performance change only due to installation of PBCF in a specific month (January). This indicates that various environmental conditions, including the wind, current, wave, etc., might influence the DHP reduction during operation of a ship.

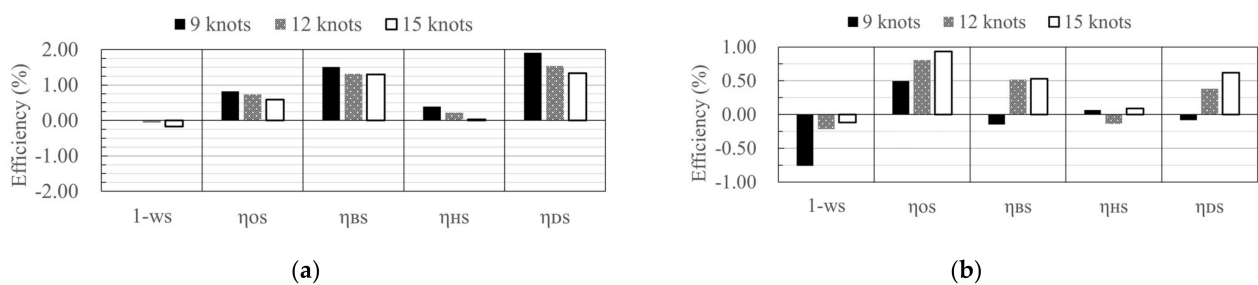


Figure 22. Effect of PBCF on the self-propulsion factors: (a) simulation and (b) experiment.

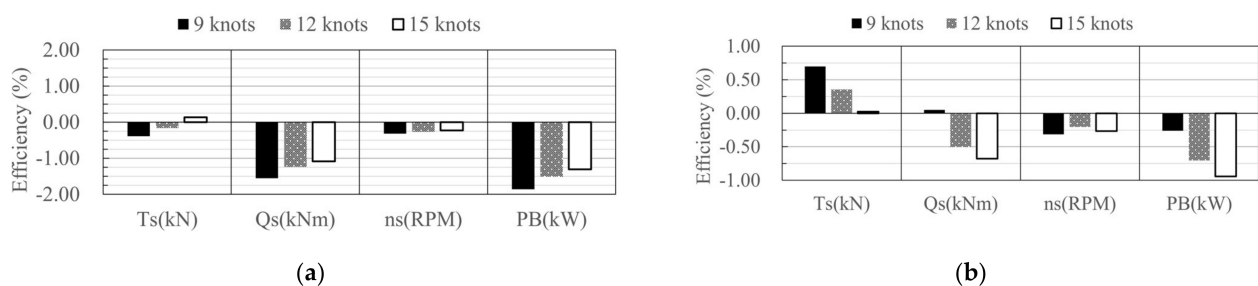
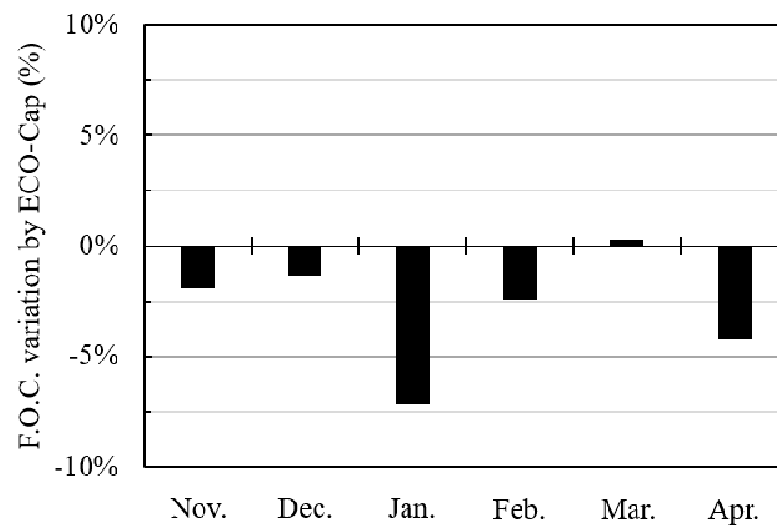


Figure 23. Effect of PBCF on the propulsion performance at full-scale: (a) simulation and (b) experiment.



**Figure 24.** Reduction of the F.O.C from full-scale measurement [11].

Accordingly, results of the present study verified that the effect of PBCF on the model-scale could be consistently estimated according to ship speed by the CFD simulation. However, it was difficult to maintain the same environmental conditions during all time for the measurement of full-scale operation or sea trial. However, simulations conducted at model-scale under a relatively consistent environment also had limitations for discussing the PBCF effect of full-scale. Thus, for accurately understand the effect of PBCF at full-scale, a full-scale simulation is required eventually. When the simulation technique for full-scale analysis can be verified and the process is precisely established, estimation of the PBCF effect is expected to be more reliable than measurement of a full-scale ship.

## 6. Conclusions

In this paper, a series of CFD simulations were performed for the resistance test, the POW test, and the self-propulsion test in order to evaluate the efficiency of PBCF under POW condition and self-propulsion conditions for a 176K bulk carrier. All analyses were performed at the model-scale. All simulations were performed with or without PBCF for the POW test and the self-propulsion test to observe the effect of PBCF. Results are as follows:

- In the resistance test, the total resistance of the 176K bulk carrier was estimated in the experiment and the simulation, showing an relative error of up to 1.2% according to the ship speed. In addition, the nominal wake was estimated similarly in the experiment and the simulation. Thus, simulation settings for self-propulsion test were designed appropriately.
- In the POW test, the POW curve with or without PBCF was estimated and a correction method was used to obtain the propeller open water performance when the PBCF was installed under the POW condition. The POW curve showed only a relative error of 2% or less between the experiment and the simulation except that the advance ratio was very high. In the POW condition, the PBCF effect was similar to the result shown in the experiment. The thrust increased by about 0.5% and the torque was decreased by 0.4%, so that the propeller open water efficiency was increased by about 1%. In the simulation result, the mechanism of PBCF was investigated using a flow field analysis. A breakdown of the hub vortex after installing PBCF was successfully observed.
- In the self-propulsion test, propulsion performance at self-propulsion point in the simulation were found to be very similar to those in the experiment, although the torque had a remarkably large relative error of 3–6%. Changes of the propulsion performance due to PBCF were relatively consistent according to ship speed in the simulation. The trend of the PBCF effect in the self-propulsion test was very similar to

the observation in the POW test. On the other hand, in the experiment, the PBCF effect at each speed did not show a consistent trend. The reason was that the amount of change in the performance by PBCF was about 0.5–1%, making it difficult to precisely measure in the model test. However, in the experiment with PBCF, the performance at the self-propulsion point also changed in a positive direction. Finally, it was found that, with PBCF, the BHP decreased by 1.5% in the simulation and by 0.5% level in the experiment.

- Exact estimation of PBCF efficiency from the model test, full-scale measurement, and sea-trial is difficult because of various environmental condition. Model-scale simulation shows a consistent trend for the PBCF effect. However, there is a fundamental problem about the scale effect. Thus, for more accurately understand the effect of PBCF at full-scale, a full-scale simulation will be required eventually.

**Author Contributions:** D.-H.K. wrote the paper and conducted CFD simulations and result analyses. Corresponding author J.-C.P. gave guidance around all works of this study and motivated student authors. G.-M.J. proofread the paper and had many discussions about results. M.-S.S. conducted the model test and gave guidance around all works, like the second correspond author. All authors have read and agreed to the published version of the manuscript.

**Funding:** This work was supported by the Technology Innovation Program (20008690, Optimal hull cleaning and propeller polishing scheduling for minimal ship operating cost using operating performance analysis) funded By the Ministry of Trade, Industry and Energy (MOTIE, Korea). This study was supported by BK21 FOUR Graduate Program for Green-Smart Naval Architecture and Ocean Engineering of Pusan National University.

**Institutional Review Board Statement:** Not applicable.

**Informed Consent Statement:** Not applicable.

**Conflicts of Interest:** The authors declare no conflict of interest. The funders had no role in the design of the study; in the collection, analyses, or interpretation of data; in the writing of the manuscript, or in the decision to publish the results.

## References

1. Smith, T.W.P.; Jalkanen, J.P.; Anderson, B.A.; Corbett, J.J.; Faber, J.; Hanayama, S.; O’Keeffe, E.; Parker, S.; Johansson, L.; Aldous, L.; et al. *Third IMO Greenhouse Gas Study*; International Maritime Organization: London, UK, 2015; Micropress Printers: Suffolk, UK, 2015.
2. Olmer, N.; Comer, B.; Roy, B.; Mao, X.; Rutherford, D. *Greenhouse Gas Emissions from Global Shipping, 2013–2015 Detailed Methodology*; The International Council on Clean Transportation: Washington, DC, USA, 2017.
3. Cames, M.; Graichen, J.; Siemons, A.; Cook, V. Emission reduction targets for international aviation and shipping. In *Policy Department A: Economic and Scientific Policy*; European Parliament: Brussels, Belgium, 2015.
4. IMO. Resolution MEPC.203(62). In *Amendments to the Annex of the Protocol of 1997 to Amend the International Convention for the Prevention of Pollution from Ships, 1973, as Modified by the Protocol of 1978 Relating Thereto*; IMO: London, UK, 2011.
5. Kawamura, T.; Ouchi, K.; Nojiri, T. Model and full scale CFD analysis of propeller boss cap fins (PBCF). *J. Mar. Sci. Technol.* **2012**, *17*, 469–480. [[CrossRef](#)]
6. Nojiri, T.; Ishii, N.; Kai, H. Energy saving technology of PBCF (Propeller Boss Cap Fins) and its evolution. *J. Jpn. Inst. Mar. Eng.* **2011**, *46*, 350–358. [[CrossRef](#)]
7. MOL Techno-Trade, Ltd. Energy-Saving Propeller Boss Cap Fins System Reaches Major Milestone—Orders Received for 3000 Vessels. Available online: <https://www.mol.co.jp/en/pr/2015/15033.html> (accessed on 14 October 2018).
8. Ouchi, K.; Ogura, M.; Kono, Y.; Orito, H.; Shiotsu, T.; Tamashima, M.; Koizuka, H. A research and development of PBCF (propeller boss cap fins). *J. Soc. Nav. Archit. Jpn.* **1988**, *1988*, 66–78. [[CrossRef](#)]
9. Ghassemi, H.; Mardan, A.; Ardeshir, A. Numerical analysis of hub effect on hydrodynamic performance of propellers with inclusion of PBCF to equalize the induced velocity. *Pol. Marit. Res.* **2012**, *19*, 17–24. [[CrossRef](#)]
10. Druckenbrod, M.; Wang, K.; Greitsch, L.; Heinke, H.J.; Abdel-Maksoud, M. Development of hub caps fitted with PBCF. In *Proceedings of the Fourth International Symposium on Marine Propulsors*, Austin, TX, USA, 31 May–4 June 2015.
11. Katayama, K.; Okada, Y.; Okazaki, A. Optimization of the Propeller with ECO-Cap by CFD. In *Proceedings of the Fourth International Symposium on Marine Propulsors*, Austin, TX, USA, 31 May–4 June 2015.
12. Park, H.J.; Kim, K.S.; Suh, S.; Park, I.R. CFD Analysis of Marine Propeller-Hub Vortex Control Device Interaction. *J. Soc. Nav. Archit. Korea* **2016**, *53*, 266–274. [[CrossRef](#)]

13. Mizzi, K.; Demirel, Y.K.; Banks, C.; Turan, O.; Kaklis, P.; Atlar, M. Design optimisation of Propeller Boss Cap Fins for enhanced propeller performance. *Appl. Ocean Res.* **2017**, *62*, 210–222. [[CrossRef](#)]
14. Kim, E.K.; Lee, K.K.; Cho, K.H. A Study on the Performance Comparison of Energy Saving Devices for Handy-size Bulk Carrier. *J. Korean Soc. Mar. Eng.* **2015**, *39*, 1–7.
15. ITTC. 1978 ITTC Performance Prediction Method. In *ITTC Report 7.5-02-03-01.4*; ITTC: Zürich, Switzerland, 2017.
16. Carrica, P.M.; Castro, A.M.; Stern, F. Self-Propulsion computations using a speed controller and a discretized propeller with dynamic overset grids. *J. Mar. Sci. Technol.* **2010**, *15*, 316–330. [[CrossRef](#)]
17. Kim, J.; Park, I.R.; Kim, K.S.; Van, S.H. RANS computation of turbulent free surface flow around a self-propelled K LNG carrier. *J. Soc. Nav. Archit. Korea* **2005**, *42*, 583–592.
18. Phillips, A.B.; Turnock, S.R.; Furlong, M. Evaluation of maneuvering coefficients of a self-propelled ship using a blade element momentum propeller model coupled to a Reynolds averaged Navier Stokes flow solver. *Ocean Eng.* **2009**, *36*, 1217–1225. [[CrossRef](#)]
19. Choi, J.E.; Min, K.S.; Kim, J.H.; Lee, S.B.; Seo, H.W. Resistance and propulsion characteristics of various commercial ships based on CFD results. *Ocean Eng.* **2010**, *37*, 549–566. [[CrossRef](#)]
20. Lee, J.H.; Park, B.J.; Rhee, S.H. Ship Resistance and Propulsion Performance Test Using Hybrid Mesh and Sliding Mesh. *J. Comput. Fluids Eng.* **2010**, *15*, 81–87.
21. Bugalski, T.; Hoffmann, P. Numerical simulation of the self-propulsion model tests. In Proceedings of the Second International Symposium on Marine Propulsors, Hamburg, Germany, 15–17 June 2011.
22. Villa, D.; Gaggero, S.; Brizzolara, S. Ship Self Propulsion with different CFD methods: From actuator disk to viscous inviscid unsteady coupled solvers. In Proceedings of the 10th International Conference on Hydrodynamics, Saint Petersburg, Russia, 1–4 October 2012.
23. Krasilnikov, V.I. Self-propulsion RANS computations with a single-screw container ship. In Proceedings of the Third International Symposium on Marine Propulsors, Tasmania, Australia, 5–8 May 2013.
24. Lungu, A. Numerical simulation of the resistance and self-propulsion model tests. In Proceedings of the ASME 2018 37th International Conference on Ocean, Offshore and Arctic Engineering, Madrid, Spain, 17–22 June 2018.
25. Kuiper, G. Cavitation Inception on Ship Propeller Models. Ph.D. Thesis, Delft University of Technology, Delft, The Netherlands, 11 March 1981.
26. Sasajima, T. A Study on the Propeller Surface Flow in Open and Behind Condition. In Proceedings of the 14th ITTC Contribution to Performance Committee, Ottawa, ON, Canada, 11 September 1975; Volume 3, p. 711.
27. Tsuda, T.; Konishi, S. Effect of Reynolds Number on Propeller Characteristics. In *Note to the ITTC Propeller Committee*; ITTC: Zürich, Switzerland, 1978.
28. ITTC. Final Report of the Propulsor Committee. In Proceedings of the 20th ITTC, San Francisco, CA, USA, 19–25 September 1993.
29. Castelli, E.B.; Raciti, M.; Grandi, G. Numerical Analysis of Laminar to Turbulent Transition on the DU91-W2-250 airfoil. *Int. J. Mech. Aerosp. Ind. Mechatron. Manuf. Eng.* **2012**, *6*, 717–724.
30. Wang, X.; Walters, K. Computational analysis of marine-propeller performance using transition-sensitive turbulence modeling. *J. Fluids Eng.* **2012**, *134*, 071107. [[CrossRef](#)]
31. Janssen, R.F. The Influence of Laminar-Turbulent Transition on the Performance of a Propeller. Master's Thesis, Delft University of Technology, Delft, The Netherlands, 24 April 2015.
32. Bhattacharyya, A.; Krasilnikov, V.; Steen, S. Scale effects on open water characteristics of a controllable pitch propeller working within different duct designs. *Ocean Eng.* **2016**, *112*, 226–242. [[CrossRef](#)]
33. Baltazar, J.; Rijpkema, D.; de Campos, J.F. On the use of the  $\gamma$ -Re $\theta$  transition model for the prediction of the propeller performance at model-scale. *Ocean Eng.* **2018**, *170*, 6–19. [[CrossRef](#)]
34. Kim, D.H.; Jeon, G.M.; Pack, J.C.; Shin, M.S. CFD Simulation on Predicting POW Performance Adopting Laminar-Turbulent Transient Model. *J. Soc. Nav. Archit. Korea* **2021**, *58*, 1–9. [[CrossRef](#)]
35. Menter, F.R.; Langtry, R.B.; Likki, S.R.; Suzen, Y.B.; Huang, P.G.; Völker, S. A correlation-based transition model using local variables—Part I: Model formulation. *J. Turbomach.* **2006**, *128*, 413–422. [[CrossRef](#)]
36. Langtry, R.B.; Menter, F.R. Correlation-Based transition modeling for unstructured parallelized computational fluid dynamics codes. *AIAA J.* **2009**, *47*, 2894–2906. [[CrossRef](#)]
37. Seok, J.; Park, J.C. Numerical simulation of resistance performance according to surface roughness in container ships. *Int. J. Nav. Archit. Ocean. Eng.* **2020**, *12*, 11–19. [[CrossRef](#)]
38. Shen, Z.; Wan, D.; Carrica, P.M. Dynamic overset grids in OpenFOAM with application to KCS self-propulsion and maneuvering. *Ocean Eng.* **2015**, *108*, 287–306. [[CrossRef](#)]
39. Ponkratov, D.; Zegos, C. Validation of ship scale CFD self-propulsion simulation by the direct comparison with sea trials results. In Proceedings of the Fourth International Symposium on Marine Propulsors, Austin, TX, USA, 31 May–4 June 2015.
40. Wang, C.; Sun, S.; Li, L.; Ye, L. Numerical prediction analysis of propeller bearing force for full-scale hull–propeller–rudder system. *Int. J. Nav. Archit. Ocean. Eng.* **2016**, *8*, 589–601. [[CrossRef](#)]
41. Jasak, H.; Vukčević, V.; Gatin, I.; Lalović, I. CFD validation and grid sensitivity studies of full scale ship self propulsion. *Int. J. Nav. Archit. Ocean. Eng.* **2019**, *11*, 33–43. [[CrossRef](#)]

- 
42. Hirt, C.W.; Nichols, B.D. Volume of fluid (VOF) method for the dynamics of free boundaries. *J. Comput. Phys.* **1981**, *39*, 201–225. [[CrossRef](#)]
  43. Muzaferija, S. A two-fluid Navier-Stokes solver to simulate water entry. In Proceedings of the 22nd symposium on naval architecture, Washington, DC, USA, 9–14 August 1999.
  44. Roache, P.J. Perspective: A method for uniform reporting of grid refinement studies. *J. Fluids Eng.* **1994**, *116*, 405–413. [[CrossRef](#)]
  45. ITTC. Guidelines: Practical Guidelines for Ship Self-Propulsion CFD. In *ITTC Report 7.5-03-03-01*; ITTC: Zürich, Switzerland, 2014.